Full Text View

Drifter Launch Strategies Based on Lagrangian Templates

A. C. Poje

Department of Mathematics, College of Staten Island, City University of New York, Staten Island, New York

M. Toner and A. D. Kirwan Jr.

Department of Marine Studies, University of Delaware, Newark, Delaware

C. K. R. T. Jones

Division of Applied Mathematics, Brown University, Providence, Rhode Island

ABSTRACT

A basin-scale, reduced-gravity model is used to study how drifter launch strategies affect the accuracy of Eulerian velocity fields reconstructed from limited Lagrangian data. Optimal dispersion launch sites are found by tracking strongly hyperbolic singular points in the flow field. Lagrangian data from drifters launched from such locations are found to provide significant improvement in the reconstruction accuracy over similar but randomly located initial deployments. The eigenvalues of the hyperbolic singular points in the flow field determine the intensity of the local particle dispersion and thereby provide a natural timescale for initializing subsequent launches. Aligning the initial drifter launch in each site along an outflowing manifold ensures both high initial particle dispersion and the eventual sampling of regions of high kinetic energy, two factors that substantially affect the accuracy of the Eulerian reconstruction. Reconstruction error is reduced by a factor of ~ 2.5 by using a continual launch strategy based on both the local stretching rates and the outflowing directions of two strong saddles located in the dynamically active region south of the central jet. Notably, a majority of those randomly chosen launch sites that produced the most accurate reconstructions also sampled the local manifold structure.

1. Introduction

- A. D. Kirwan
- C. K. R. T. Jones

Lagrangian data from drifters and floats has become an increasingly important tool in studying the ocean's circulation on a variety of scales. In particular, drogued drifter data provide velocity observations at depth: essential information for the latest generation of prognostic ocean models, which depend heavily on observational input for initialization, data assimilation, and model validation (see, e.g., Davis 1991; Stutzer and Krauss 1998; Smith et al. 2000). Increasingly, the combined need for accurate real-time ocean observations and the expense of deploying observational arrays demands a priori optimization of observational resources. The basic question is which of a necessarily limited number of initial launch locations provide measurements that most accurately capture the ocean state?

The problem of designing optimal ocean observing systems is inherently difficult, requiring global solutions of a very high dimensional, nonlinear, and constrained optimization. Formal treatments based on statistical techniques such as a generalized inverse approach, extended Kalman filters (Bennett 1990), and simulated annealing (Barth and Wunsch 1990) have been successfully applied to a number of specific problems involving fixed observing stations (see, e.g., McIntosh 1987; Barth 1992; Hackert et al. 1998).

When the data in question come from Lagrangian floats, the design problem is further complicated by advection of the observing sites. In a given experiment, drifter launch sites are typically chosen via a combination of statistical reasoning and operational convenience. However, a number of efforts have addressed optimizing the location of drifter launch sites given some supplemental knowledge of the flow field. Treshnikov et al. (1986), in a basin-scale study of the South Atlantic, proposed maximizing a collection of functionals based on the spatial degree of the initial data coverage and averaged quantities including kinetic energy and enstrophy. Their results indicate optimal reconstruction of the Eulerian surface current field when drifters are preferentially seeded in high kinetic energy regions such as Drake Passage. Using both time-dependent model and fixed observational velocity fields to advect numerical drifters, Hernandez et al. (1995) employ a genetic algorithm to determine globally optimal drifter launch locations in a region of the Azores Current. For single release experiments, optimal launch locations are those that ensure high data coverage at the time of data analysis. Typically, this implies seeding high kinetic energy regions with initial drifter separation determined by local properties of the velocity field. As the time between launch and analysis is increased, optimal launch locations tend to straddle persistent coherent structures since such deployments ensure drifters are not advected out of the region before the analysis time.

In this paper, our goal is to establish a criterion that requires a minimal amount of a priori information for selecting drifter launch locations. We require only knowledge of the dynamic-height field at launch time. In practice, such information would be available from altimeter data or near–real-time ocean models.

Our long-term goal is to reconstruct Eulerian flow fields from Lagrangian and disparate Eulerian data. The reconstruction technique involves objectively mapping the data onto geometrical orthogonal functions (GOFs), also referred to as normal mode analysis (NMA: Lipphardt et al. 2000; Toner et al. 2001). Here, we test our launch strategies with simulated data from a reduced gravity, double gyre flow. The energetics of the basin-scale flow are dominated by long lived, mesoscale structures such as rings and jets. These Eulerian structures have corresponding Lagrangian structures that are defined by inflowing and outflowing manifolds emanating from hyperbolic (saddle) trajectories (see, e.g., Miller et al. 1997; Poje and Haller 1999; Rogerson et al. 1999). These time-dependent entities mark the Lagrangian boundaries of the coherent structures and orchestrate drifter motion.

As observed in Treshnikov et al. (1986) and Hernandez et al. (1995) and shown in the numerical experiments of Toner et al. (2001), reconstruction accuracy is a strong function of the coverage afforded by the drifter data. In addition to coverage, previous work indicates increasing accuracy when drifters sample high KE regions of the flow. With this as a basis for producing accurate reconstructions, we propose a general launch strategy based on initially seeding drifters in the vicinity of strong hyperbolic points identified from dynamic height data. Drifters launched in such regions should provide improved Eulerian reconstructions for two reasons. First, such drifters experience extremely high initial dispersion owing to the high local material stretching rates. Large dispersion rates ensure the highest level of drifter coverage in the shortest period of time from launch time. Second, drifters launched in hyperbolic regions will rapidly sample energetic areas of the flow. This seems counterintuitive since hyperbolic regions are typically associated with regions of low velocity. However, high kinetic energy regions are typically foliated with the outflowing manifolds of the hyperbolic trajectories; hence drifters launched around a hyperbolic point will preferentially explore high velocity regions of the flow.

This launch strategy also provides a rational means for building up longer-term observations. The initial drifter behavior is dominated by the saddle dynamics of the hyperbolic point, and the eigenvalues of the linearization around this point provide a natural and dynamic timescale for determining when drifters should be relaunched.

To compare the accuracy of velocity reconstructions using drifters launched near hyperbolic trajectories, two ensembles of experiments are performed. First, we study a single time release of drifters directed along the outflowing direction of persistent saddle points in the flow. Comparison to an ensemble of random reference launches establishes the characteristics

of drifter launch locations indicative of reduced reconstruction error.

The second ensemble of experiments focuses on reseeding the flow with drifters. In the directed launches, drifters are released at saddle points with relaunching times based on the local stretching rates determined from the hyperbolicity of the saddle. This strategy combines a directed launch strategy with an eventual optimal observation scenario, namely that drifters end up located uniformly along the boundaries of the coherent structures marked by the outflowing manifolds. The effectiveness of this strategy is judged in comparison to an ensemble of similar, randomly initialized experiments.

Section 2 describes the flow and the Lagrangian structures that will form the basis of the launch strategy. The technique used to reconstruct the model Eulerian velocity, and therefore assess the quality of the drifter deployments, is described in section 3. The single release experiment along the outflowing eigenvectors is compared to random deployments in section 4. The results of the single release experiments are used to formulate the time-dependent launch strategy, which is described and similarly compared to random deployments in section 5. The work is summarized in section 6.

2. Model flow and Lagrangian dynamics

As a convenient model for oceanic mesoscale currents, we consider a single-layer, reduced-gravity equation set subjected to double gyre wind forcing:

$$\frac{\partial u}{\partial t} + u\frac{\partial u}{\partial x} + v\frac{\partial u}{\partial y} - f_0(1 + \beta y)v = -g'\frac{\partial h}{\partial x} + F^u + \nu\nabla^2 u$$

$$\frac{\partial v}{\partial t} + u\frac{\partial v}{\partial x} + v\frac{\partial v}{\partial y} + f_0(1 + \beta y)u = -g'\frac{\partial h}{\partial y} + F^v + \nu\nabla^2 v$$

$$\frac{\partial h}{\partial t} + \frac{\partial(uh)}{\partial x} + \frac{\partial(vh)}{\partial y} = 0. \tag{1}$$

The domain is a 2000 km by 2000 km box with uniform 10-km spatial resolution. Subgrid-scale stresses are modeled by a standard, constant eddy-viscosity Laplacian term with no-slip conditions imposed at the boundaries. The double gyre is set up by imposing a wind stress (F^u, F^v) given by

$$F^u = \frac{\tau_0}{\rho H_0} \sin\left(\frac{2\pi y}{L_y}\right)$$

and $F^v = 0$. The exact parameter values employed are given in Table 1 ⊙. Details of the numerical scheme, adapted from Poje et al. (1996), are given in Poje and Haller (1999).

A representative 120 day time period of velocity and height data is archived once per simulation day several model years after spinup. A time stamp of "Day 1" is assigned to the first archived field.

Figure 1 ⊙ shows contours of the dynamic height field and the location of two Eulerian saddle points on day 45 of the simulation. In general, the flow is characterized by a strong, eddy-shedding central jet and a dynamically active subtropical gyre where we concentrate our study. In this region, the fluctuating component of the Eulerian velocity field is dominated by highly energetic and relatively long-lived coherent structures in the form of eddies shed from the jet. Such Eulerian structures in turn govern the Lagrangian drifter dynamics on intermediate ($\sim$ weekly/monthly) timescales. We will concentrate on optimizing drifter based reconstructions on these timescales.

Idealizing drifters or floats as purely Lagrangian fluid particles, the equations for the trajectory of a drifter are simply

$$\frac{dx}{dt} = u(x, y, t) \qquad \frac{dy}{dt} = v(x, y, t), \tag{2}$$

subject to initial conditions $(x(t_0), y(t_0)) = (x_0, y_0)$.

Throughout, the ordinary differential equations given by (2) are solved using a LSODA routine from the public domain

library ODEPACK with variable time stepping and internal error checking. The numerically generated velocity field is found at the particle position using bicubic spatial and linear temporal interpolation schemes.

Under certain conditions (see Haller and Poje 1998), the presence of saddle-type equilibria in fixed time slices of the Eulerian velocity field implies the existence of nearby hyperbolic trajectories in the full, time-dependent Lagrangian flow. Emanating from these trajectories are a pair of dynamically significant material curves (invariant manifolds) characterized by strong compression and stretching of nearby Lagrangian trajectories. One of these curves, the inflowing or stable manifold, consists of trajectories that tend toward the hyperbolic trajectory in forward time while the other, the outflowing or unstable manifold, consists of all trajectories tending toward the hyperbolic trajectory in backward time.

Such invariant curves act as Lagrangian boundaries to the coherent flow features (see, e.g., MacKay et al. 1984; Rom-Kedar et al. 1990; Jones and Winkler 2001). The near-exponential stretching in the neighborhood of the hyperbolic trajectory ensures maximal relative particle dispersion for drifter pairs that straddle this point.

For finite time datasets, the invariant manifolds and the location of the hyperbolic trajectory can be computed given the location and strength of a saddle point in the Eulerian flow for intermediate times τ between initial, t_i, and final, t_f, times. For fixed time saddle equilibria given by

$$\begin{pmatrix} u(x(\tau),\ y(\tau),\ \tau) \\ v(x(\tau),\ y(\tau),\ \tau) \end{pmatrix} = \mathbf{0},$$

the strength of the hyperbolicity is determined by the eigenvalues $\lambda(\tau)$ of the Jacobian matrix

$$J = \begin{pmatrix} \partial u/\partial x & \partial u/\partial y \\ \partial v/\partial x & \partial v/\partial y \end{pmatrix}_{(x(\tau),y(\tau),\tau)}.$$

Operationally, for slowly evolving geophysical flows, the conditions given in Haller and Poje (1998) for the existence of hyperbolic trajectories in the neighborhood of the saddle, $(x(\tau),\ y(\tau),\ \tau)$, require that the rate of change of both the location of the saddle and the associated eigendirection be small compared to typical particle speeds and that the Lagrangian timescales be much faster than the timescale of the Eulerian evolution,

$$d\lambda/d\tau \ll \lambda^2,$$

where λ is the positive eigenvalue of the Jacobian matrix evaluated at the saddle point. These conditions are typically satisfied by energetic eddies interacting with both the central jet and the western boundary current in the double-gyre model flow (Poje and Haller 1999).

Figure 2 ⊙⁼ indicates both the eigenvectors of the western saddle depicted in Fig. 1 ⊙⁼ and the location of the corresponding invariant manifolds in the Lagrangian flow for the model velocity field. The manifolds were constructed using the straddling technique developed in Miller et al. (1997). As shown in the figure, the unstable manifold is formed by initializing a *seed* curve along the unstable eigenvector at time t_i and integrating forward in time. As the curve stretches, new trajectories are added in order to maintain uniform particle density along the curve. The stable manifold is constructed similarly, initializing along the stable eigenvector at time t_f and integrating backward in time. The hyperbolic trajectory, identified by the intersection of stable and unstable manifolds, remains near the saddle point for all times. For intermediate times, when both manifolds are sufficiently formed, they mark the Lagrangian boundary between two eddies in the subtropical gyre.

As shown in Fig. 3 ⊙⁼, the hyperbolic trajectory has a significant, global influence on the particle dynamics. Using the location of the Eulerian saddle as a guide, two material curves are integrated in forward time. The disc initialized around the saddle (and hence enclosing the hyperbolic trajectory) is rapidly stretched in the direction of the unstable manifold. Locally, in the neighborhood enclosing the hyperbolic trajectory, solutions are dominated by the saddle dynamics and spread exponentially. Considering the relative spread of two trajectories, $\mathbf{r}(t) = \mathbf{x}_1(t) - \mathbf{x}_2(t)$,

$$\mathbf{r}(t) \sim \mathbf{r}_0 e^{\bar{\lambda}t},$$

where $\bar{\lambda} = t^{-1}\int_0^t \lambda(\tau)d\tau$ is the average hyperbolicity during the integration time. Since these initial conditions straddle the hyperbolic point, this high stretching persists throughout the integration. For comparison, a second disc is initialized 40 km

away from the saddle. These trajectories also stretch rapidly along one branch of the unstable manifold as they move away from the hyperbolic trajectory. The relative dispersion does not, however, monotonically increase. As seen in the final frame of Fig. 3 ⟳, trajectories for this second disc are eventually compressed as they return along the stable manifold towards the hyperbolic point. As stated in the introduction, our goal is to use these properties of the Lagrangian dynamics to direct our choice of initial drifter launch locations.

While the model velocity field results from a reduced-gravity shallow-water model, the instantaneous zonal and meridional velocities are adequately approximated by the geostrophic relations (Poje and Haller 1999; Toner et al. 2001),

$$\tilde{u} = -\frac{g'}{f}\frac{\partial h}{\partial y}, \qquad \tilde{v} = \frac{g'}{f}\frac{\partial h}{\partial x}, \qquad (3)$$

where g' and f are the model-dependent reduced gravity and Coriolis parameters. The geometry of the Lagrangian dynamics linearized about a hyperbolic trajectory is then, at any time, governed by the Hessian of the instantaneous height field,

$$H = \begin{pmatrix} \partial^2 h/\partial x^2 & \partial^2 h/\partial x\partial y \\ \partial^2 h/\partial x\partial y & \partial^2 h/\partial y^2 \end{pmatrix}. \qquad (4)$$

Consequently, the location and eigenvectors of saddle points can be found without direct knowledge of the velocity field or the value of the reduced gravity parameter. The eigenvalues, and the local expansion rates, are known from the height field up to a multiplicative constant.

3. Eulerian reconstruction

Eulerian velocity fields are objectively reconstructed from drifter data using the spectral approach given by Rao and Schwab (1981), Eremeev et al. (1995a,b), and Lipphardt et al. (2000). A three-dimensional velocity field is split into two scalar potentials,

$$\mathbf{u} = \nabla \times [-\mathbf{k}\Psi + \nabla \times (\mathbf{k}\Phi)], \qquad (5)$$

where $\mathbf{k}$ is a unit vector in the vertical direction. Projection on the vertical component of relative vorticity results in a Helmholtz equation for Ψ with homogeneous boundary conditions,

$$\nabla^2 \psi_n + \lambda_n \psi_n = 0, \qquad \psi_n|_{\text{boundary}} = 0.$$

Similarly, projection on the vertical velocity component results in a Helmholtz equation for Φ with Neumann boundary conditions,

$$\nabla^2 \phi_m + \lambda_m \phi = 0, \qquad \left.\frac{\partial \phi_m}{\partial n}\right|_{\text{boundary}} = 0,$$

where $\partial/\partial n$ is the derivative normal to the boundary. Given the geometry of the flow domain, these two equations can be solved for the eigenfunctions ψ_i and ϕ_j, which represent the two-dimensional incompressible (streamfunction) and divergent modes respectively. The two dimensional velocity field can then be written as

$$u(\mathbf{x}, t) = \sum_{n=1}^{N} -A_n(t)\frac{\partial \psi_n(\mathbf{x})}{\partial y} + \sum_{m=1}^{M} B_m(t)\frac{\partial \phi_m(\mathbf{x})}{\partial x}$$

$$v(\mathbf{x}, t) = \sum_{n=1}^{N} A_n(t)\frac{\partial \psi_n(\mathbf{x})}{\partial x} + \sum_{m=1}^{M} B_m(t)\frac{\partial \phi_m(\mathbf{x})}{\partial y}.$$

The model flow considered allows several simplifications. The rectangular geometry implies that the eigenmodes are simply sines and cosines. In the parameter range considered, the velocity fields are dominated by quasigeostrophic dynamics. As shown in Toner et al. (2001), projections on the divergent, velocity potential modes contain relatively little

energy and will be neglected in the present reconstructions.

Under these assumptions, reconstruction of the Eulerian field at any time reduces to a least squares minimization of the fitting coefficients $A_n(t)$. Given an array of drifter observations,

$$\mathbf{o} = \begin{pmatrix} u_{ob}(\mathbf{x}_1(t), t) \\ u_{ob}(\mathbf{x}_2(t), t) \\ (\\ v_{ob}(\mathbf{x}_2(t), t) \\ v_{ob}(\mathbf{x}_2(t), t) \\ (\end{pmatrix},$$

at M locations $\mathbf{x}_i = (x_i, y_i)$, the N unknown coefficients $\mathbf{a} = [A_1, \cdots, A_N]$ be found by minimizing

$$\| \mathbf{Ga} - \mathbf{o} \|_2$$

with respect to $\mathbf{a}$. The matrix elements in $\mathbf{g}$ are

$$G_{ij} = -\frac{\partial \psi_i(\mathbf{x}_j)}{\partial y}$$

for the u velocity components and

$$G_{ij} = \frac{\partial \psi_i(\mathbf{x}_j)}{\partial x}$$

for the v velocity components.

We measure reconstruction error by the kinetic energy of the difference velocity normalized by the kinetic energy of the model velocity within the subdomain D,

$$E(t) = \iint_D (\mathbf{u}_{model} - \mathbf{u}_{recon})^2 \, dA \Big/ \iint_D (\mathbf{u}_{model})^2 \, dA.$$

Based on the results of Toner et al. (2001) for this flow, we choose $N = 15 \times 15$ half-wavenumbers across the full basin. With this spectral discretization, the model velocities can be reproduced with less than 5% error by taking observations at every second model grid point.

In order to concentrate on comparing launch strategies in the subdomain of interest and to reduce the total number of drifter required for reasonably accurate reconstructions, we uniformly sample the flow outside the subdomain at 97 fixed grid points as shown in Fig. 1 ⊙. These observations augment the drifter data launched in the subdomain. Given the 225 basis functions and the 194 fixed observations, the least squares procedure requires a minimum of 16 drifters (32 observations) to reproduce the Eulerian velocities.

4. Single release results

The relative improvement in reconstruction accuracy achieved by using velocity data from drifters launched along the outflowing direction of saddles within the flow is quantified by comparing the reconstruction error of these launches to the error of similar, random launches. Data projected on the GOF basis functions consists of 20 drifters launched within the active subdomain and 97 uniformly spaced moorings located in the exterior, quiescent region (see Fig. 1 ⊙). On day 45, two strong saddles in the subdomain are used for the "directed" deployment strategy. Two launch patterns, each consisting of ten drifters spaced at 10 km intervals, are deployed straddling each saddle and oriented parallel to the corresponding outflowing direction. To gauge the effectiveness of the directed launch strategy, 100 random deployments are launched on

the same day within the subdomain. These comparative deployments each consist of two 100 km line segments, the center and alignment of which are chosen randomly.

In Fig. 4 ⊙, time series of reconstruction error are shown for those experiments which achieve the minimum error (of all 101) during the ten days following launch. The directed launch along unstable eigenvectors, experiment 101, achieves the minimum error of the ensemble on day 54, nine days after deployment. The error histograms of all 101 experiments are shown in Fig. 5 ⊙ for three different times. For reference, the reconstruction error E for each experiment shown in Fig. 4 ⊙ is indicated in the histograms shown in Fig. 5 ⊙. Initially, the error distribution is concentrated about the mean. As time evolves, the distribution flattens considerably due to dispersion.

The time dependence of the reconstruction error illustrates the difference between optimal observing and optimal deployment strategies. Note that in Fig. 4 ⊙, experiment 51 has the minimum error ($\sim 50\%$) upon deployment but, after two days, does not maintain that status. In particular, note that the error from experiment 101 is initially high, since the drifters are in low kinetic energy regions, but is reduced significantly as the drifters advect to the higher kinetic energy regions along the unstable manifolds.

In order to understand which drifter properties reduce reconstruction error, three statistical measures,

Lagrangian kinetic energy:

$$KE = \frac{1}{n_d}\left(\sum_{i=1}^{n_d} u_i^2 + v_i^2\right),$$

relative dispersion:

$$D = \frac{1}{n_d}\left(\sum_{i=1}^{n_d} (\mathbf{x}_i - \bar{\mathbf{x}}_i)^2\right),$$

coverage:

$$C = \sum_{k=1}^{n_b} \alpha(B_k, \mathbf{x}_1, \cdots, \mathbf{x}_{n_d}),$$

are computed for each experiment in the ensemble. Here n_d is the number of drifters in an experiment ($n_d = 20$); $\mathbf{x}_1, \ldots$, $\mathbf{x}_{n_d}$ and $u_i, v_i, \ldots$, u_{n_d}, v_{n_d} represent the drifter positions and velocity components (the time dependence is suppressed); n_b is the number of bins into which the subdomain is partitioned in order as to identify coverage; $B_1, \ldots$, B_{n_b} are the corresponding bins; and $\alpha(B_k, \mathbf{x}_1, \ldots$, $\mathbf{x}_{n_d}) = 1$ if any of the drifters are within B_k and zero otherwise. For this flow, the 1200 km $\times$ 700 km subdomain D is partitioned into 17 $\times$ 10 cells to form 170 bins. The cell size, ~ 70 km, corresponds roughly to twice the Rossby radius.

Scatterplots of KE, D, and C versus E are shown in Fig. 6 ⊙ on day 54. We denote the linear correlation coefficient between two statistical measures a and b of the ensemble as corr(a, b). While corr(KE, E), corr(D, E), and corr(C, E) are all negative, corr(KE, E) is the strongest. As expected, the directed launch has the highest relative dispersion and the highest coverage. The scatterplot for coverage indicates that there is considerable variability in error for low coverage experiments. The directed deployment experiment (experiment 101) has the highest coverage, highest relative dispersion and lowest error, but not the highest kinetic energy. However, note that experiment 54 has only a slightly higher reconstruction error, very low coverage, but very high kinetic energy and relative dispersion. Similarly, experiment 94 has relatively low reconstruction error, relatively high kinetic energy, but rather low dispersion. Clearly, no one statistic exclusively indicates low reconstruction error, but the trend is clear.

To understand the transition between an optimal observation and an optimal deployment, corr(KE, E), corr(D, E), and corr(C, E) are computed daily. The resulting time series, for the period up to ten days after launch, are shown in Fig. 7 ⊙. Here corr(KE, E) remains relatively high throughout the period, indicating the persistent influence of high kinetic energy, while corr(D, E) is initially low, but increases steadily. The maximum coverage that may be obtained in this series of experiments is 20 (out of 170), so even the best of the deployments will be a low coverage experiment. The time series of corr(C, E) confirms the variable nature of this statistic for these experiments. However, the continuous release results given

in section 5, indicate that this statistic is quite significant when 40 drifters are launched allowing differentiation between "high" and "low" coverage samples.

Common characteristics in launch locations of the five minimum error experiments are shown in Fig. 8 ⊙, where the individual drifter locations are superimposed on the location of manifolds for three different days. At launch time, each of the experiments has at least one of the two line segments straddling a manifold; three of the four most accurate random launch sites initialize a segment in the neighborhood of one of the strong saddle points. All of the experiments (with the possible exception of experiment 58) evolve such that a majority of drifters are located in high shear, high velocity regions of the flow. This corroborates the results in Figs. 6 and 7 ⊙.

The single release results indicate that deployments which maximize relative dispersion, Lagrangian kinetic energy, and eventual coverage should provide improved Eulerian reconstructions. The directed launch experiment produces the lowest reconstruction error nine days after launch. Figure 4 ⊙ shows, however, that the reconstruction error for the directed launch increases on the tenth day after launch. Thus, while near optimal for times comparable to the exponential dispersion times, the directed launches are suboptimal for longer times. A directed launch strategy with reseeding is considered next.

5. Continuous release results

Based on the results of single time release experiments, a time-dependent launch strategy may be formulated that explicitly incorporates the saddle dynamics. Assuming geostrophy, the eigenvalues of the Hessian matrix (4) multiplied by the reduced gravity parameter g'/f produce an inverse timescale indicating the strength of the hyperbolicity associated with each saddle.

The estimated hyperbolicity of each saddle is used to determine when a drifter launched along the outflowing direction (or simply launched nearby) will leave the region. Since the flow field near these saddles is dominated by the local linear structure there, the positive eigenvalues approximate the amount of time needed for the drifter to travel exponentially away from the saddle. For example, if the positive eigenvalue of a saddle is $\lambda = 1/3$ day^{-1}, then a drifter launched 20 km along the unstable eigenvector will be approximately 54 km away from the saddle in three days [20 km $\times$ exp(1/3 day^{-1} $\times$ 3 day)]. If another drifter were launched 20 km on the other side of the saddle along the other outflowing direction at the same time, then the distance between the two would be approximately 108 km, assuming the manifolds have not yet curved. By reseeding the saddle after three days with a drifter in each outflowing direction, the approximate distance between drifters flowing in the same direction would be 34 km. However, this grows to 94 km after three more days, assuming the positive eigenvalue remains $\lambda = 1/3$ day^{-1}. As the exponential stretching along the unstable manifold typically decays as drifters move away from the hyperbolic region, eventually a nominal separation distance between drifters is maintained for successively launched drifters.

This scenario outlines the basic elements of the continuous release launch strategy. Reseeding times are based on the time-dependent hyperbolicity of each saddle, and thus result in a relatively uniform sample of the outflowing manifolds. Time series of the saddle timescales for the two saddles used in section 4 are shown in Fig. 9 ⊙. The eastern saddle appears on day 18 and maintains a relatively constant eigenvalue with timescales of approximately 6 days. The western saddle, initially weak, strengthens during the first 25 days before weakening considerably for a short time due to the interaction with an eddy shed from the jet.

Similar to the single release strategy in section 4, two drifters are launched 40 km apart, one on either side of the saddle with the two aligned in the outflowing direction. This is repeated every $1/\lambda$ days (the e-doubling time for displacement away from the saddle in the linearized flow) during a 41-day period ending on day 48. Seeding of the western saddle begins on day 7 and continues until day 48. The eastern saddle forms on day 17 and is seeded until day 46. Reseeding times for each saddle are rounded up to the next day (for convenience) resulting in the launch of 36 drifters, 22 deployed near the western saddle (with a mean reseeding time of 4.2 days) and 14 deployed near the eastern saddle (with a mean reseeding time of 4.8 days). Actual reseeding times are shown by symbols in Fig. 9 ⊙.

Since the four eddy centers will not be sampled with the outflowing manifolds, additional drifters are added at the eddy centers on the last day of the saddle launch. The eddy centers are estimated by the location of the appropriate elliptic stagnation points on day 48. Although the extra four drifters do not sample high kinetic energy regions, they remove the data voids inherent in the saddle launch strategy.

To assess the effectiveness of the continuous launch strategy, 100 random launch experiments that incorporate the same basic elements are performed. For each reference experiment, two random locations are chosen (within the subdomain) to simulate the saddles with one associated (for launch purposes) with the western and the other associated with the eastern saddle. Random drifter pairs are launched 40 km apart at the same time as the directed drifters. At each launch, the orientation of the pair is randomly chosen. The center of each drifter pair is translated in a random direction the same distance as an actual saddle moves between reseeding times. Finally, on day 48, four additional drifters are launched

randomly in the subdomain.

Time series of the reconstruction error from day 48 to day 54 for the three experiments that produce minimum error are shown in Fig. 10 ⊙. The directed deployment, experiment 101, maintains a low reconstruction error throughout this time period. Note that on days 50, 51, and 52 the minimum error experiments change from experiment 55 to experiment 101 to experiment 62. Histograms of E for the last launch day and these three days, shown in Fig. 11 ⊙, indicate a peaked error distribution with only a few experiments in the low error tail. In particular, only the error from the directed deployment consistently remains in the lowest error bin.

The proximity of drifters to the manifold structures in the flow indicate the benefit of sampling these regions. Figure 12 ⊙ shows the drifter locations of the minimum error experiments on days 50–52. The directed deployment, shown in Fig. 12b ⊙, samples the outflowing manifolds well, as expected. However, drifters in both experiment 55 and experiment 62 are in very close proximity to the manifolds. In particular, drifters in experiment 62 are much better displaced along the unstable manifolds than those of experiment 55. This is the likely reason that error from experiment 55 is much more variable than the error from experiment 62.

It should be noted that the experiments with the maximum error (not shown) all sample in the quiescent regions of the flow, while experiments with mean error (also not shown) tend to have some sampling of the manifold structure.

The statistics KE and C defined in section 4 are computed, and a scatterplot of both KE versus E and C versus E are shown for day 53 in Fig. 13 ⊙. The correlations corr(KE, E) and corr(C, E) are typical for the 7-d period. With the increased number of drifters, coverage becomes a more significant diagnostic as compared to the single release results shown in Figs. 6 and 7 ⊙. As with the single release results, the correlation between reduced reconstruction error and sampling high kinetic energy regions remains relatively persistent and high.

To put the directed continual launch strategy in perspective, a comparison is made with both a uniform initial distribution of 40 drifters launched on day 7 (the first of the continual launches) and a uniform Eulerian sample of 40 moorings. Figure 14 ⊙ shows the time series of E for all reconstructions. Error from the continual launch is not shown until day 28, when enough drifters are launched to perform the minimization in a least squares sense. Clearly, until the continual launch deployment produces the same number of drifters (on day 48), the uniform initial distribution of drifters has much lower error. However, during the 7-day period following the last launch, reconstruction error from the directed strategy is not only lower than the error from the uniform launch, it is only slightly higher than error from the uniformly distributed Eulerian sample.

6. Conclusions

A drifter launch strategy is designed that incorporates the Lagrangian dynamics of the velocity field near persistent saddles in the Eulerian flow field. High dispersion rates near these saddles result from a nearby hyperbolic trajectory, from which emanates an outflowing (unstable) manifold that delineates and controls particle dynamics in and around adjacent coherent structures. These manifolds connect the low kinetic energy region, where the drifters were launched, to high kinetic energy regions of the coherent structure boundaries.

In the double-gyre test case, we concentrated on reconstructing the Eulerian velocity field in a dynamically active region south of the jet. The reconstruction error was then used to judge the quality of the drifter deployment. Two strong saddles located there were used to direct drifter deployments in both a single release and continual release launch strategy. In both cases, launches directed along the outflowing direction of the saddles resulted in significantly reduced reconstruction error compared to similar, random launches. In addition to trends that indicate kinetic energy, dispersion, and coverage were all important in reduced reconstruction error, the random experiments with the lowest reconstruction error all launched drifters either near a saddle or across a manifold structure. Similarly, random launches from the continual release experiments indicate that when drifters sample the manifold structure the reconstruction error is reduced.

The directed single release experiment relied only on knowledge of the height field in the model. This is advantageous since, in an operational guise, velocities will not be known directly. The more accurate continual release results relied on knowledge of the reduced gravity parameter to estimate reseeding times. By reseeding the saddles, a relatively uniform concentration of drifters along the unstable manifolds of both saddles was achieved. An empirical relation between spatial gradients of the height field near saddle regions and the local velocity there should give similar results. An additional deployment in the continual release strategy was used to sample eddy centers located by tracking elliptic points in the height field. Since outflowing manifolds typically provide strong transport barriers to eddy interiors, these additional launches effectively eliminate data voids.

Reconstruction error from the directed, continual launch strategy approaches the error of the uniform mooring sampling seven days after the final release (see Fig. 14 ⊙). After that, however, the error increases and then oscillates in a similar

fashion to the reconstruction error obtained from the drifters that were launched en masse from a uniform grid at the time of the continual launch experiment. This implies, as is the case with the single release experiments, that the "optimal" nature of deployments are fleeting. To maintain low reconstruction error, newly formed saddles must be used as the older saddles weaken.

The directed launch strategy relies on locating hyperbolic Lagrangian particle trajectories in time-dependent Eulerian fields. For the model flow and particular domain considered here, the methods of Haller and Poje (1998), based on the connection between fixed-time saddle points and hyperbolic trajectories in flows with slowly varying, adiabatic Eulerian structures, is adequate. Figure 2b ⊙ clearly indicates that the correspondence between the Eulerian eigenstructure and the Lagrangian manifold structure is not exact. However, bounds for the distance between the two are given in Haller and Poje (1998) and can be computed directly from the Eulerian data (note, for example, the strong relationship between the strength of the hyperbolicity shown in Fig. 9 ⊙ and the distance between the hyperbolic trajectory and saddle point in Fig. 2 ⊙). For the two strong saddle points considered here, the initial drifter separation of 100 km in the single release results is more than adequate to mask the uncertainty in the location of the hyperbolic point relative to the Eulerian saddle at launch time (see Fig. 2c ⊙).

For flows with more general time dependence, including flows without the appearance of saddle points in fixed time slices of the Eulerian field or flows subject to high local rotation rates, controlling hyperbolic trajectories may still exist. Determining the location of such Lagrangian trajectories may, however, require more involved methods than those used here. Recently a number of efforts have addressed this issue (see, e.g., Haller 2001, personal communication; for a recent review). Typically, these techniques involve either direct maximization of the relative Lagrangian dispersion (Bowman 1999; Jones and Winkler 2001) or the computation of frame independent invariants of the local Lagrangian rate of strain along trajectories (Lapeyre et al. 1999; Haller 2000; Haller and Yuan 2000). Using such techniques, essential hyperbolic Lagrangian structures have been identified in a variety of relatively complex flows including energetic two-dimensional turbulence, the stratospheric circumpolar vortex and analytic, three-dimensional ABC flows.

While we have used an idealized flow in this study since the manifold structure was previously examined (Poje and Haller 1999), application to a more natural setting is an important next step. Kuznetzov et al. (2001, manuscript submitted to *J. Mar. Res.*) recently identified hyperbolic regions and computed finite-time manifolds in the eastern Gulf of Mexico. Location of hyperbolic trajectories in the context of this data-assimilating, multilayer ocean model is more challenging, but will provide an important next step toward operational experiments.

REFERENCES

Barth N., 1992: Oceanographic experiment design. II: Genetic algorithms. *J. Atmos. Oceanic Technol.*, **9**, 434–443. Find this article online

Barth N., and C. Wunsch, 1990: Oceanographic experiment design by simulated annealing. *J. Phys. Oceanogr.*, **20**, 1249–1263. Find this article online

Bennett A., 1990: *Inverse Methods in Physical Oceanography*. Cambridge University Press, 346 pp.

Davis R., 1991: Observing the general-circulation with floats. *Deep-Sea Res.*, **38**, 531–571. Find this article online

Davis R., L. Ivanov, A. D. Kirwan Jr., and T. Margolina, 1995a: Amount of ^{137}Cs and ^{134}Cs radionuclides in the Black Sea produced by the Chernoboyl accident. *J. Environ. Radioact.*, **27**, 49–63. Find this article online

Davis R., 1995b: Analysis of caesium pollution in the Black Sea by regularization methods. *Mar. Pollut. Bull.*, **7**, 460–462. Find this article online

Hackert E., R. Miller, and A. Busalacchi, 1998: An optimized design for a moored instrument array in the tropical Atlantic Ocean. *J. Geophys. Res.*, **103**, 7491–7509. Find this article online

Haller G., 2000: Finding finite-time invariant manifolds in two-dimensional velocity fields. *Chaos*, **10**, 99–108. Find this article online

Haller G., 2001: Lagrangian coherent structures and the rate of strain in two-dimensional turbulence. *Phys. Fluids.*, **13**, 3365–3385. Find

this article online

Haller G., and A. Poje, 1998: Finite time transport in aperiodic flows. *Physica D*, **119**, 352–380. Find this article online

Haller G., and G.-C. Yuan, 2000: Lagrangian coherent structures and mixing in two-dimensional turbulence. *Physica D*, **147**, 352–370. Find this article online

Hernandez F., P.-Y. Le Traon, and N. H. Barth, 1995: Optimizing a drifter cast strategy with a genetic algorithm. *J. Atmos. Oceanic Technol.*, **12**, 330–345. Find this article online

Jones C., and S. Winkler, 2001: Do invariant manifolds hold water? *Handbook of Dynamical Systems III: Towards Applications,* G. B. Fiedler and N. Kopell, Eds., Elsevier.

Lapeyre G., P. Klien, and B. Hua, 1999: Does the tracer gradient vector align with the strain eigenvectors in 2D turbulence? *Phys. Fluids*, **11**, 3729–3737. Find this article online

Lipphardt B., A. D. Kirwan Jr., C. Grosch, J. Lewis, and J. Paduan, 2000: Blending HF radar and model velocities in Monterey Bay through normal mode analysis. *J. Geophys. Res.*, **105**, 3425–3450. Find this article online

MacKay R., J. Meiss, and I. Percival, 1984: Transport in Hamiltonian systems. *Physica D*, **13**, 55–81. Find this article online

McIntosh P., 1987: Systematic design of observational arrays. *J. Phys. Oceanogr.*, **17**, 885–902. Find this article online

Miller P., C. Jones, A. Rogerson, and L. Pratt, 1997: Quantifying transport in numerically generated velocity fields. *Physica D*, **110**, 105–122. Find this article online

Poje A., and G. Haller, 1999: Geometry of cross-stream mixing in a double-gyre ocean model. *J. Phys. Oceanogr.*, **29**, 1649–1665. Find this article online

Poje A., D. Jones, and L. Margolin, 1996: Enslaved finite-difference schemes for quasi-geostrophic, shallow flows. *Physica D*, **98**, 559–573. Find this article online

Rao D., and D. Schwab, 1981: A method of objective analysis for currents in a lake with applications to Lake Ontario. *J. Phys. Oceanogr.*, **11**, 739–750. Find this article online

Rogerson A., P. Miller, L. Pratt, and C. Jones, 1999: Lagrangian motion and fluid exchange in a barotropic meandering jet. *J. Phys. Oceanogr.*, **29**, 2635–2655. Find this article online

Rom-Kedar V., A. Leonard, and S. Wiggins, 1990: An analytical study of transport, mixing and chaos in an unsteady vortical flow. *J. Fluid Mech.*, **214**, 347–394. Find this article online

Smith R., M. Maltrud, F. Bryan, and M. W. Hecht, 2000: Numerical simulation of the North Atlantic Ocean at $\frac{1}{10}°$. *J. Phys. Oceanogr.*, **30**, 1532–1561. Find this article online

Stutzer S., and W. Krauss, 1998: Mean circulation and transports in the South Atlantic Ocean: Combining model and drifter data. *J. Geophys. Res.*, **103**, 30985–31002. Find this article online

Toner M., A. Poje, A. D. Kirwan Jr., C. K. Jones, B. L. Lipphardt, and C. E. Grosch, 2001: Reconstructing basin-scale Eulerian velocity fields from simulated drifter data. *J. Phys. Oceanogr.*, **31**, 1361–1376. Find this article online

Treshnikov A., V. Guretskiy, A. Danilov, N. Yefremeyev, L. Ivanov, and V. Smelyanskiy, 1986: Optimal array of satellite-tracked drifting buoys in the Southern Alantic. *Dokl. Akad. Nauk SSSR*, **287**, 430–434. Find this article online

Tables

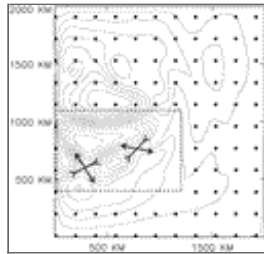TABLE 1. Parameter values for the numerical model

| Coriolis parameter	$f_0 = 6.0 \times 10^{-5}\ s^{-1}$
$f = f_0(1 + \beta y)$	$\beta = 0.66\ (2.00 \times 10^{-11}\ 1\ ms^{-1})$
Wind stress	$\tau_0 = 0.1\ N\ m^{-2}$
Viscosity parameter	$\nu = 175\ m^2\ s^{-1}$
Reduced gravity	$g' = 0.02\ m\ s^{-2}$
Nominal layer depth	$H_0 = 500\ m$

Click on thumbnail for full-sized image.

Figures

FIG. 1. Dynamic height field in the reduced gravity model on day 45. Depth ranges from 400 to 700 m with contour intervals of 20 m. The experimental subdomain is located within the dotted lines. The 97 fixed, exterior sample points are shown by the solid dots. Resolution of the exterior sample grid is 190 km
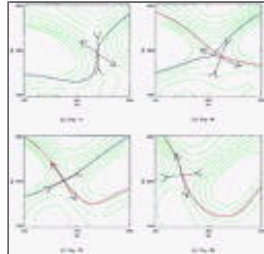
FIG. 2. Evolution of material curves that form the invariant manifolds. The unstable (stable) manifold is formed by the red (blue) curve initialized along the unstable (stable) eigenvector and integrated forward (backward) in time beginning on day 15 (60)
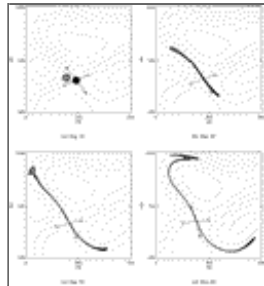
FIG. 3. Two material curves, discs of radius 20 km, are initialized near the saddle. The curve centered on the saddle deforms along the outflowing manifold while the adjacent curve translates with minimal stretching
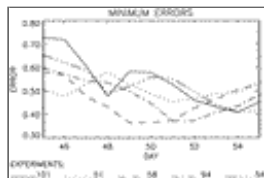
FIG. 4. Time series of the reconstruction error for the five experiments that produce minimum error during the ten days following drifter launch
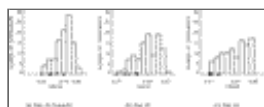
FIG. 5. Error histograms for the ensemble of single release experiments. Five minimum error experiments are shown: 101 (•), 51 (×), 58 (△), 94 (*), and 54 (□). Experiment 101 is the directed launch experiment

FIG. 6. Scatterplots of kinetic energy, relative dispersion, and coverage vs reconstruction error for the single release experiments nine days after launch (day 54). Larger symbols represent the experiments identified in Fig. 5 ⟳
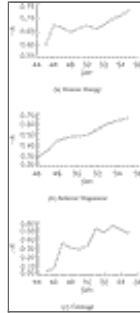
FIG. 7. Time series of the correlation between error and drifter characteristics for the single release experiments. At each time, the linear correlation coefficient between reconstruction error and kinetic energy, relative dispersion, or coverage is computed for the ensemble
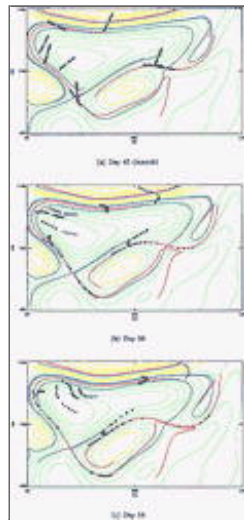
FIG. 8. The location of drifters for the minimum error experiments shown in Fig. 4 ⟳. Symbols correspond to those in Fig. 5 ⟳. Stable (blue) and unstable (red) manifolds are shown along with contours of the height field.
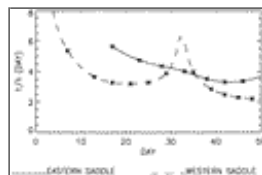
FIG. 9. Time series of timescales given by the inverse of the hyperbolicity of the two saddle points used as launch sites. Symbols denote reseeding times used in the continuous release experiment
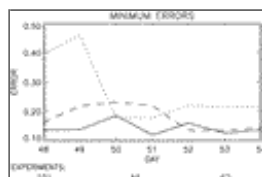
FIG. 10. Time series of the reconstruction error in the continuous release experiment. Shown are the three experiments that produce minimum error during the 10 days following the final drifter launch
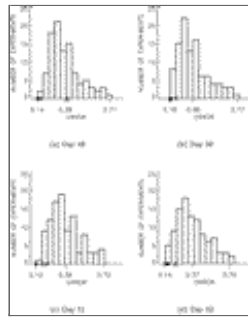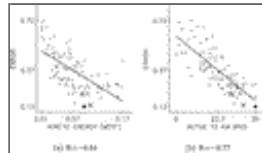
Click on thumbnail for full-sized image.

FIG. 11. Error histograms of the continuous release experiments on days when expt 101 (•), expt 55 (△), and expt 62 (×) achieve minimum reconstruction error
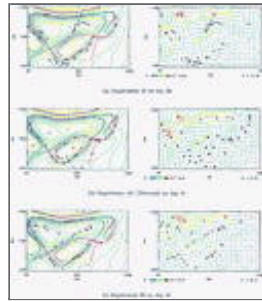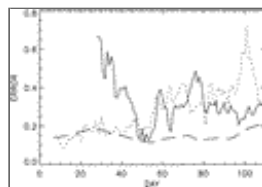

Click on thumbnail for full-sized image.

FIG. 12. The manifold structure and drifter locations (left) along with the reconstructed velocity field (right) of the experiments in Fig. 10 ⊙▬. The days shown are those when each deployment gives the minimum reconstruction of the ensemble

Click on thumbnail for full-sized image.

FIG. 13. Scatterplots of kinetic energy, and coverage vs reconstruction error for the continuous release experiments seven days after the final launch (day 53). Larger symbols represent the experiments identified in Fig. 11 ⊙▬

Click on thumbnail for full-sized image.

FIG. 14. Time series of errors from the directed deployment (solid line) and the uniform deployment (dotted line) of 40 drifters on day 7. For comparison, error from 40 uniformly distributed moorings is also shown (dashed line)

Corresponding author address: Dr. A. C. Poje, Dept. of Mathematics, College of Staten Island, CUNY, Staten Island, NY 10314. E-mail: poje@math.csi.cuny.edu